

## PERPENDICULAR ION HEATING BY REDUCED MAGNETOHYDRODYNAMIC TURBULENCE

QIAN XIA<sup>1</sup>, JEAN C. PEREZ<sup>1,2</sup>, BENJAMIN D. G. CHANDRAN<sup>1</sup>, & ELIOT QUATAERT<sup>3</sup>

*Draft version July 24, 2018*

### ABSTRACT

Recent theoretical studies argue that the rate of stochastic ion heating in low-frequency Alfvén-wave turbulence is given by  $Q_{\perp} = c_1[(\delta u)^3/\rho] \exp(-c_2/\varepsilon)$ , where  $\delta u$  is the rms turbulent velocity at the scale of the ion gyroradius  $\rho$ ,  $\varepsilon = \delta u/v_{\perp i}$ ,  $v_{\perp i}$  is the perpendicular ion thermal speed, and  $c_1$  and  $c_2$  are dimensionless constants. We test this theoretical result by numerically simulating test particles interacting with strong reduced magnetohydrodynamic (RMHD) turbulence. The heating rates in our simulations are well fit by this formula. The best-fit values of  $c_1$  are  $\sim 1$ . The best-fit values of  $c_2$  decrease (i.e., stochastic heating becomes more effective) as the grid size and Reynolds number of the RMHD simulations increase. As an example, in a  $1024^2 \times 256$  RMHD simulation with a dissipation wavenumber of order the inverse ion gyroradius, we find  $c_2 = 0.21$ . We show that stochastic heating is significantly stronger in strong RMHD turbulence than in a field of randomly phased Alfvén waves with the same power spectrum, because coherent structures in strong RMHD turbulence increase orbit stochasticity in the regions where ions are heated most strongly. We find that  $c_1$  increases by a factor of  $\sim 3$  while  $c_2$  changes very little as the ion thermal speed increases from values  $\ll v_A$  to values  $\sim v_A$ , where  $v_A$  is the Alfvén speed. We discuss the importance of these results for perpendicular ion heating in the solar wind.

*Subject headings:* Sun: corona — (Sun:) solar wind — waves — plasmas — turbulence

### 1. INTRODUCTION

Beginning in the 1950s, a number of authors developed hydrodynamic models of the solar wind with heating from thermal conduction (Parker 1958, 1965; Roberts & Soward 1972; Durney 1972). For realistic values of the coronal density and temperature, these models led to wind speeds near Earth of  $\sim 300$  km/s (Durney 1972), much smaller than the speeds of 700 – 800 km/s that are observed in the fast solar wind. In addition, in two-fluid (proton plus electron) models in which thermal conduction is the only heating mechanism, the proton temperatures near Earth are much smaller than the observed proton temperatures (Hartle & Sturrock 1968). These discrepancies imply that the fast solar wind is heated by some mechanism(s) other than thermal conduction.

Some clues into the nature of this additional heating are provided by measurements of ion temperatures. In-situ spacecraft measurements show that  $T_{\perp p} > T_{\parallel p}$  in low- $\beta$  fast-solar-wind streams, where  $\beta = 8\pi p/B^2$  is the ratio of the plasma pressure to the magnetic pressure, and  $T_{\perp p}$  ( $T_{\parallel p}$ ) is the perpendicular (parallel) temperature of the protons, which measures the speed of thermal motions in directions perpendicular (parallel) to the magnetic field (Marsch et al. 1982b). Remote observations from the Ultraviolet Coronagraph Spectrometer show that the temperature of heavy ions is much larger than the proton temperature in coronal holes (Kohl, J., et al. 1998; Esser et al. 1999). In addition,  $T_{\perp} \gg T_{\parallel}$  for O<sup>+5</sup> ions in coronal holes at heliocentric distances  $r$  of  $\sim 2R_s$ , where  $R_s$  is the solar radius (Antonucci et al. 2000). These observations show that, when  $\beta \ll 1$ , ions experience strong perpendicular heat-

ing and heavy ions are heated preferentially.

One possible mechanism for explaining these ion-temperature signatures is Alfvén waves (AWs) or AW turbulence (Coleman 1968). Propagating AWs are seen in infrared observations of the solar corona (Tomczyk et al. 2007). AW-like motions are also seen in optical observations of the low corona, and the speeds of these motions imply an outward AW energy flux sufficient to power the solar wind (De Pontieu et al. 2007). Farther from the Sun, fluctuations in the magnetic field, electric field, and average proton velocity are consistent with a broad spectrum of turbulent, Alfvén-wave-like fluctuations, in the sense that there is a rough equipartition between the fluctuating magnetic energy and kinetic energy over a broad range of scales (Tu & Marsch 1995; Goldstein et al. 1995; Bale et al. 2005). A hallmark of three dimensional turbulence, in hydrodynamic fluids as well as magnetized plasmas, is the cascade of fluctuation energy from large scales to small scales or, equivalently, from small wavevectors  $k$  to large wavevectors (Kolmogorov 1941; Iroshnikov 1963; Kraichnan 1965). The frequency of a linear AW is  $k_{\parallel}v_A$ , where  $k_{\parallel}$  ( $k_{\perp}$ ) is the component of  $k$  parallel (perpendicular) to the magnetic field,

$$v_A = \frac{B}{\sqrt{4\pi n_{\text{proton}} m_p}} \quad (1)$$

is the (proton) Alfvén speed,  $n_{\text{proton}}$  is the proton density, and  $B$  is the magnetic field strength. If AW energy cascades to sufficiently large  $k_{\parallel}$ , then the wave frequency will become comparable to the cyclotron frequencies of ions, and strong ion cyclotron heating will result (Isenberg & Hollweg 1983; Hollweg & Isenberg 2002). In principle, such cyclotron heating could account for the perpendicular ion heating discussed above.

There is, however, a problem with the above scenario. When turbulent AWs interact in strongly turbulent plasmas, their energy cascades primarily to larger  $k_{\perp}$ , and only weakly to larger  $k_{\parallel}$  (Shebalin et al. 1983; Goldreich & Sridhar

<sup>1</sup> Space Science Center and Department of Physics, University of New Hampshire, Durham, NH; qdy2@unh.edu, benjamin.chandran@unh.edu

<sup>2</sup> Department of Physics, University of Wisconsin at Madison, 1150 University Avenue, Madison, WI 53706, USA; jcperez@wisc.edu

<sup>3</sup> Astronomy Department & Theoretical Astrophysics Center, 601 Campbell Hall, The University of California, Berkeley, CA 94720, USA; eliot@astro.berkeley.edu

1995). As a consequence, the small-scale waves produced by the anisotropic AW cascade are unable to cause cyclotron heating (Quataert 1998; Cranmer & van Ballegoijen 2003; Howes et al. 2008a). If the small-scale waves produced by the cascade were to damp via linear wave damping, they would lead primarily to parallel electron heating in the low- $\beta$  conditions of the solar corona, and to virtually no ion heating.

This discrepancy has led a number of authors to go beyond linear wave theory in analyzing the dissipation of AW turbulence. (e.g., Voitenko & Goossens 2004; Dmitruk et al. 2004; Markovskii et al. 2006; Parashar et al. 2009; Lehe et al. 2009; Lynn et al. 2012; Servidio et al. 2011a). In this paper, we investigate a nonlinear heating mechanism called “stochastic heating,” which arises when fluctuating electric and/or magnetic fields at wavelengths comparable to a particle’s gyroradius disrupt a particle’s smooth gyromotion, leading to the non-conservation of the particle’s magnetic moment (McChesney et al. 1987; Johnson & Cheng 2001; Chen et al. 2001; Chaston et al. 2004; Fiksel et al. 2009; Chandran 2010). Chandran et al. (2010) derived an analytic formula for the stochastic ion heating rate  $Q_{\perp\text{stoch}}$  in plasmas with  $\beta \lesssim 1$  as a function of the turbulence amplitude at the gyroradius scale. Their formula (Equation (4) below) contains two dimensionless constants. Chandran et al. (2010) simulated test-particles interacting with randomly phased AWs and kinetic Alfvén waves (KAWs) to evaluate these constants. In this work, we re-evaluate these constants by simulating test-particles interacting with strong reduced magnetohydrodynamic (RMHD) turbulence. The remainder of this paper is organized as follows. We briefly review previous work on stochastic ion heating and strong RMHD turbulence in Sections 2 and 3. We then discuss our numerical methods in Section 4, present our results in Section 5, and summarize our conclusions in Section 6.

## 2. STOCHASTIC ION HEATING

If an ion moves in the presence of electric and magnetic fields that vary over a characteristic spatial scale  $l$  and time scale  $\tau$ , and if the ion’s gyroradius  $\rho$  and cyclotron frequency  $\Omega_i$  satisfy the inequalities  $\rho \ll l$  and  $\Omega_i \tau \gg 1$ , then the ion’s motion in the plane perpendicular to  $\mathbf{B}$  is nearly periodic. As a consequence, the ion’s magnetic moment  $\mu = mv_{\perp}^2/2B$ , an adiabatic invariant, is almost exactly conserved (Kruskal 1962). Here,  $m$  is the ion’s mass,  $v_{\perp}$  is the component of the ion’s velocity perpendicular to  $\mathbf{B}$ ,  $\Omega_i = qB/mc$ ,  $q$  is the ion charge,  $c$  is the speed of light, and  $\rho = v_{\perp}/\Omega_i$ . On the other hand, if  $l \sim \rho$ , and if the amplitudes of the fluctuations in the electric and/or magnetic fields are sufficiently large, then the ion’s motion in the plane perpendicular to  $\mathbf{B}$  ceases to be nearly periodic, even if  $\Omega_i \tau \gg 1$ , and magnetic moment conservation is violated (McChesney et al. 1987). In this case, the velocity-space average of the ion magnetic moment,  $k_B T_{\perp}/B$ , can increase in time. Perpendicular heating resulting from the disruption of particle gyro-orbits by turbulent fluctuations with  $\Omega_i \tau$  significantly greater than unity is called stochastic heating.

Chandran et al. (2010) derived an analytic formula for the stochastic ion heating rate in anisotropic AW/KAW turbulence, in which the fluctuating quantities vary rapidly in directions perpendicular to the background magnetic field and slowly in the direction parallel to the background magnetic field. The assumptions in their derivation apply to RMHD turbulence even in the absence of the kinetic physics that mod-

ifies linear waves at lengthscales smaller than the proton gyroradius  $\rho_p$ . Chandran et al. (2010) considered a Maxwellian distribution of ions with temperature  $T_i$ , perpendicular thermal speed

$$v_{\perp i} = \left( \frac{2k_B T_i}{m} \right)^{1/2}, \quad (2)$$

and thermal-particle gyroradius

$$\rho_i = v_{\perp i}/\Omega_i. \quad (3)$$

Using phenomenological arguments, these authors derived the following analytic formula for the stochastic ion heating rate (per unit mass) for the case in which  $\beta \lesssim 1$ :

$$Q_{\perp\text{stoch}} = \frac{c_1 (\delta u)^3}{\rho_i} \exp\left(-\frac{c_2}{\varepsilon_i}\right), \quad (4)$$

where  $c_1$  and  $c_2$  are dimensionless constants,

$$\varepsilon_i = \frac{\delta u}{v_{\perp i}}, \quad (5)$$

$$\delta u = \left[ \int_{k_{-}}^{k_{+}} E_u(k_{\perp}) dk_{\perp} \right]^{1/2}, \quad (6)$$

$k_{\pm} = e^{\pm 0.5}/\rho_i$  and  $E_u(k_{\perp})$  is the 1D power spectrum of the  $\mathbf{E} \times \mathbf{B}$  velocity of the plasma ( $c\mathbf{E} \times \mathbf{B}/B^2$ ). The normalization of  $E_u(k_{\perp})$  is chosen so that  $\int_0^{\infty} E_u(k_{\perp}) dk_{\perp}$  is the total mean square  $\mathbf{E} \times \mathbf{B}$  velocity. Thus,  $\delta u$  is the rms amplitude of the  $\mathbf{E} \times \mathbf{B}$  velocity or “fluid velocity” at scale  $\rho_i$ . Chandran et al. (2010) numerically simulated stochastic heating of test particles by a spectrum of randomly phased AWs and KAWs whose spectra are drawn from the critical-balance model (Goldreich & Sridhar 1995; Cho & Lazarian 2004), for the case in which  $\beta \ll 1$ . Their numerically computed heating rates agreed well with Equation (4) with  $c_1 = 0.75$  and  $c_2 = 0.34$ . However, they argued that stochastic heating is more efficient at fixed  $\delta u$  in strong AW/KAW turbulence than in a randomly phased wave field, implying a larger value of  $c_1$  and/or smaller value of  $c_2$ , because strong AW/KAW turbulence produces coherent structures that increase orbit stochasticity (Dmitruk et al. 2004). In this paper, we test this argument and obtain new values of  $c_1$  and  $c_2$  for the case of test particles interacting with strong RMHD turbulence.

When the perpendicular length scale  $\lambda_{\perp}$  of a turbulent “eddy” or “wave packet” is  $\sim \rho_i$ , the cascade time in “balanced” (i.e., zero-cross-helicity) RMHD turbulence is  $\tau_{\lambda} \sim \rho_i/\delta u$ . Thus,  $\varepsilon_i \simeq (\Omega_i \tau_{\lambda})^{-1}$ . For critically balanced turbulence, the linear frequency  $\omega_A = k_{\parallel} v_A$  is comparable to the nonlinear frequency  $\tau_{\lambda}^{-1}$  (Goldreich & Sridhar 1995; Boldyrev 2005). Combining the above relations, we obtain

$$\omega_A \sim \varepsilon_i \Omega_i. \quad (7)$$

Equation (7) can be used to estimate the relative importance of stochastic heating and cyclotron heating for particles interacting with small-amplitude, randomly phased AWs or KAWs with  $k_{\perp} \rho_i \sim 1$ , where the wave frequencies are chosen to satisfy the critical-balance condition  $\omega \sim \rho_i/\delta u$ . Assuming that the imaginary part of the frequency is much less than the real part, each ion species makes a contribution  $\gamma_i$  to the total wave damping rate that can be expressed analytically (Kennel & Wong 1967). If an ion species has an isotropic Maxwellian distribution with thermal speed  $v_{\perp i}$ ,

then  $\gamma_i \propto e^{-\zeta^2}$ , where  $\zeta = (\omega - \Omega_i)/k_{\parallel}v_{\perp i}$ . In writing this expression, we have retained only the contribution to  $\gamma_i$  from the lowest cyclotron harmonic, which is dominant because we assume  $\omega \ll \Omega_i$ . This exponential factor is proportional to the number of particles whose parallel velocities satisfy the wave-particle resonance condition  $\omega - k_{\parallel}v_{\parallel} = n\Omega_i$  with  $n = 1$ . Using Equation (7) and the inequality  $\omega \ll \Omega_i$ , we obtain  $\zeta^2 \sim 1/(\beta_i \varepsilon^2)$ , where

$$\beta_i \equiv \frac{v_{\perp i}^2}{v_A^2}. \quad (8)$$

Because the energy gained by the particles equals the energy lost by the waves, we can obtain a rough estimate of the ratio of the cyclotron heating rate  $Q_c$  to the stochastic heating rate  $Q_{\perp}$  by comparing just the exponential factors in the expressions for  $Q_c$  and  $Q_{\perp}$ , which yields  $Q_c/Q_{\perp} \sim \exp(c_2 \varepsilon^{-1} - \zeta^2)$ . This implies that  $Q_c \ll Q_{\perp}$  when  $\varepsilon \beta_i \ll 1$ , indicating that cyclotron heating becomes increasingly subdominant to stochastic heating as  $\varepsilon$  and/or  $\beta_i$  decreases. To the extent that arguments from linear wave theory describe cyclotron heating by strong AW/KAW turbulence, the above discussion also implies that  $Q_c \ll Q_{\perp}$  in strong AW/KAW turbulence when  $\varepsilon \beta_i \ll 1$ .

We note that the theory of Chandran et al. (2010) does not in general apply to electrons. It is assumed in that theory that the dominant contribution to the stochastic heating rate comes from fluctuations with perpendicular lengthscales comparable to the particle gyroradii, and that these gyroradii are  $\gtrsim \rho_p$ . In plasmas with electron temperatures that are comparable to the proton temperature, the thermal-electron gyroradii are  $\ll \rho_p$ . Energetic electrons could have gyroradii  $\gtrsim \rho_p$ , but the value of  $\varepsilon$  for such electrons would be extremely small, indicating that stochastic heating of these fast electrons would be exponentially weak.

### 3. STRONG RMHD TURBULENCE

As described in the introduction, we consider test particles interacting with strong reduced magnetohydrodynamic (RMHD) turbulence. The main assumptions of RMHD are that: (1) the fluctuating magnetic field  $\delta \mathbf{B}$  is much smaller than the background magnetic field  $\mathbf{B}_0$ ; (2)  $\delta \mathbf{B}$  and the fluctuating fluid velocity  $\delta \mathbf{u}$  are perpendicular to  $\mathbf{B}_0$  (i.e., the fluctuations are “transverse”); (3)  $\nabla \cdot \mathbf{u} = 0$ ; (4) the fluctuations vary much more rapidly in directions perpendicular to  $\mathbf{B}_0$  than the direction parallel to  $\mathbf{B}_0$  ( $k_{\perp} \gg |k_{\parallel}|$ ); (5) the perpendicular lengthscales are much larger than the proton gyroradius  $\rho_p$ , and (6) the frequencies of the fluctuations are much smaller than the proton cyclotron frequency (Kadomtsev & Pogutse 1974; Strauss 1976; Zank & Matthaeus 1992; Schekochihin et al. 2009). Although RMHD is a fluid theory, it is a good approximation for transverse, low-frequency, non-compressive fluctuations with  $k_{\perp} \gg |k_{\parallel}|$  even in collisionless plasmas such as the solar wind (Schekochihin et al. 2009). However, in some cases, such as the solar wind at  $r = 1$  AU, RMHD is applicable only at lengthscales that are sufficiently small that  $|\delta \mathbf{B}| \ll B_0$ .

In full (as opposed to reduced) magnetohydrodynamics (MHD), there are three propagating waves: the Alfvén wave (AW), the fast magnetosonic wave, and the slow magnetosonic wave. RMHD retains only one of these linear wave modes, the AW. We thus at times refer to RMHD turbulence as AW turbulence. We recognize that not all types

of AW turbulence can be described within the framework of RMHD. In particular, Alfvén-wave fluctuations with  $|k_{\parallel}| \gtrsim k_{\perp}$  do not satisfy the assumptions of RMHD. However, our focus is on strong, anisotropic AW turbulence, which satisfies  $k_{\perp} \gg |k_{\parallel}|$  at scales much smaller than the driving scale (Goldreich & Sridhar 1995; Maron & Goldreich 2001; Perez & Boldyrev 2008).

The equations of RMHD can be expressed in terms of the Elsässer variables

$$\mathbf{z}^{\pm} = \mathbf{u} \mp \mathbf{b}, \quad (9)$$

where  $\mathbf{b} = \delta \mathbf{B} / \sqrt{4\pi\rho_0}$  and  $\rho_0$  is the mass density. These equations take the form

$$\frac{\partial \mathbf{z}^{\pm}}{\partial t} \pm (\mathbf{v}_A \cdot \nabla) \mathbf{z}^{\pm} + (\mathbf{z}^{\mp} \cdot \nabla) \mathbf{z}^{\pm} = -\nabla P + \nu \nabla^2 \mathbf{z}^{\pm} + \mathbf{f}^{\pm} \quad (10)$$

$$\nabla \cdot \mathbf{z}^{\pm} = 0, \quad (11)$$

and

$$\mathbf{z}^{\pm} \cdot \mathbf{B}_0 = 0, \quad (12)$$

where  $\mathbf{v}_A = \mathbf{B}_0 / \sqrt{4\pi\rho_0}$  is the Alfvén velocity,  $P = (p/\rho_0 + b^2/2)$ ,  $p$  is the plasma pressure,  $\nu$  is the viscosity (which we have taken to be equal to the resistivity), and  $\mathbf{f}^{\pm}$  is an external driving force, which we include as a source term for turbulence. Both  $\rho_0$  and  $\mathbf{B}_0$  are taken to be constant.

The properties of RMHD turbulence have been studied extensively with the use of direct numerical simulations (Dmitruk et al. 2003, 2005; Perez & Boldyrev 2008, 2009; Mason et al. 2012; Perez et al. 2012). These simulations find that AW energy cascades from large perpendicular scales to small perpendicular scales, ultimately dissipating at a small scale, which we call the “Kolmogorov scale,” in analogy to hydrodynamic turbulence. Scales much smaller than the energy-injection scale but much larger than the Kolmogorov scale are referred to as the “inertial range of scales.” As in hydrodynamic turbulence, the breadth of the inertial range increases with increasing Reynolds number  $\text{Re} = u_{\text{rms}} L_{\perp} / \nu$ , where  $u_{\text{rms}}$  is the rms amplitude of the velocity, and  $L_{\perp}$  is the lengthscale characterizing the forcing term. In “balanced” RMHD turbulence, in which there is equal energy in  $z^+$  fluctuations and  $z^-$  fluctuations, the inertial-range power spectrum of the total energy (kinetic plus magnetic) is proportional to  $k_{\perp}^{-3/2}$  in simulations of strong RMHD turbulence (Perez & Boldyrev 2008). However, the velocity power spectrum  $E_u(k_{\perp})$  is flatter than the total-energy spectrum (i.e.,  $\propto k_{\perp}^{-n}$  with  $n < 3/2$ ), while the magnetic power spectrum is somewhat steeper than the total-energy spectrum (Boldyrev et al. 2011, 2012).

### 4. NUMERICAL METHOD

Our basic numerical method is to solve the RMHD equations in a periodic, 3D domain using a pseudo-spectral code, and to numerically integrate the orbits of test particles that propagate within the time-varying electromagnetic fields produced by the 3D RMHD simulations. In the following two subsections, we describe the details of our numerical algorithms.

#### 4.1. The RMHD Code

To solve the RMHD equations, we use the pseudo-spectral ‘‘RMHD Code’’ (Perez & Boldyrev 2008). The numerical domain of this code is a 3D box with periodic boundary conditions. The background (mean) magnetic field in the simulation,  $\mathbf{B}_0$ , is along the  $z$  axis, where  $(x, y, z)$  are Cartesian coordinates. We define  $k_\perp = \sqrt{k_x^2 + k_y^2}$ . That is, we define  $k_\perp$  with respect to the mean magnetic field. (In contrast, as discussed below, we define the the test-particle velocity components  $v_\perp$  and  $v_\parallel$  with respect to the local magnetic field direction.)

The lengths of the box in the  $x$ ,  $y$ , and  $z$  directions are, respectively,  $L_\perp, L_\perp$ , and  $L_\parallel$ , where  $L_\parallel/L_\perp = 6$ . The simulations are run for a long enough time so that the turbulence reaches an approximate statistical steady state, and the driving term  $\mathbf{f}^\pm$  is chosen so that the rms fluctuating velocity

$$u_{\text{rms}} = \left[ \int_0^\infty E_u(k_\perp) dk_\perp \right]^{1/2} \quad (13)$$

is approximately  $v_A/5$ . Therefore,

$$\chi = \frac{v_A L_\perp}{u_{\text{rms}} L_\parallel} \simeq 1, \quad (14)$$

which means the turbulence is in critical balance at the outer scale (Goldreich & Sridhar 1995). Moreover, as we discuss further below, the RMHD equations are invariant when  $L_\parallel$  and  $v_A$  are both multiplied by the same factor  $\xi$ . We take advantage of this fact to enable a single simulation to appear as different turbulent fields (with different scaling factors  $\xi$ ) to different cohorts of test particles.

The driving forces  $\mathbf{f}^\pm$  lie in the  $xy$  plane, are solenoidal and nonzero only at small wavenumbers satisfying  $2\pi/L_\perp \leq k_\perp \leq 4\pi/L_\perp$  and  $2\pi/L_\parallel \leq k_\parallel \leq 4\pi/L_\parallel$ . We assign random values (drawn from a Gaussian distribution) to each nonzero Fourier component of  $\mathbf{f}^\pm$  at selected times  $t_n = nt_{\text{force}}$ , where  $n = -1, 0, 1, 2, \dots$ , and choose  $t_{\text{force}} = \tau/5$  so that the coefficients are refreshed 5 times every eddy turnover time  $\tau = L_\perp/(2\pi\delta u)$ . Between these discrete times, such as  $t \in (t_{n+1}, t_{n+2})$ , we determine the value of  $\mathbf{f}^\pm(t)$  by cubic interpolation, using the values of  $\mathbf{f}^\pm(t_n), \mathbf{f}^\pm(t_{n+1}), \mathbf{f}^\pm(t_{n+2})$  and  $\mathbf{f}^\pm(t_{n+3})$ . We include  $t_{-1}$ , so that we can begin cubic interpolation at the beginning of the simulation at  $t = 0$  with the desired value for  $\mathbf{f}^\pm(t = 0)$ , which is set to zero in this work. The time step  $\delta t$  of the RMHD simulations is constrained by a Courant condition to ensure numerical stability and is much smaller than  $t_{\text{force}}$ .

## 4.2. Particle Tracing

We introduce test particles into the RMHD simulations after a time of at least  $10L_\perp/u_{\text{rms}}$  has elapsed, so that the turbulence has reached a statistical steady state in which the rate of viscous dissipation matches (on average) the rate at which the forcing term adds energy into the flow. We neglect Coulomb collisions and track each particle’s velocity  $\mathbf{v}$  and position  $\mathbf{x}$  by solving the equations

$$\frac{d\mathbf{x}}{dt} = \mathbf{v} \quad (15)$$

and

$$\frac{d\mathbf{v}}{dt} = \frac{q}{m} \left( \mathbf{E} + \frac{\mathbf{v} \times \mathbf{B}}{c} \right), \quad (16)$$

where  $\mathbf{E}$  is the electric field and  $\mathbf{B}$  is the magnetic field. As when solving the RMHD equations, we use periodic boundary conditions when tracing particle orbits. If a particle leaves the simulation domain through one boundary, it re-enters the box from the corresponding point on the opposite boundary.

In order to simulate perpendicular heating accurately, we want to minimize the risk that our code artificially violates  $\mu$  conservation through numerical error. Lehe et al. (2009) showed that a fourth-order Runge-Kutta integration of Equations (15) and (16) leads to a secular decrease in particle energy and magnetic moment in the presence of a uniform magnetic field and zero electric field. In particular, when they used ten time steps per gyration, the particle energy decreased by 1% per gyration. We thus reject that method as unsuitable for this problem. Instead, we follow Lehe et al. (2009) and others in using the ‘‘Boris-pusher’’ method (Boris 1970), which differs Equations (15) and (16) at time  $t_i = i\Delta t$  ( $i = 0, 1, 2, \dots$ ) according to the scheme

$$\frac{\mathbf{x}_{i+1} - \mathbf{x}_i}{\Delta t} = \mathbf{v}_{i+1/2} \quad (17)$$

and

$$\frac{\mathbf{v}_{i+1/2} - \mathbf{v}_{i-1/2}}{\Delta t} = \frac{q}{m} \mathbf{E}_i + \frac{q}{mc} \frac{\mathbf{v}_{i+1/2} + \mathbf{v}_{i-1/2}}{2} \times \mathbf{B}_i. \quad (18)$$

Equation (18) can be re-written as

$$\mathbf{v}^+ - \mathbf{v}^- = (\mathbf{v}^+ + \mathbf{v}^-) \times \frac{\Delta t q}{2mc} \mathbf{B}_i \quad (19)$$

with:  $\mathbf{v}^\pm = \mathbf{v}_{i\pm 1/2} \mp \Delta t q/2m \mathbf{E}_i$ . Upon taking the dot product of Equation (19) with  $\mathbf{v}^+ + \mathbf{v}^-$ , one finds that  $|\mathbf{v}^+|^2 = |\mathbf{v}^-|^2$ . Thus, when  $\mathbf{E} = 0$ , the Boris-pusher method conserves particle energy to machine precision.

We evaluate  $\mathbf{E}$  in the RMHD simulations using the idealized Ohm’s Law,

$$\mathbf{E} = -\frac{\mathbf{u}}{c} \times \mathbf{B}. \quad (20)$$

We interpolate the electric and magnetic fields from the grid points to each particle’s position. We follow Lehe et al. (2009) in using the triangular-shaped cloud (TSC) method to interpolate the field information in 4 dimensions (both space and time). To avoid introducing an artificial component of  $\mathbf{E}$  parallel to the local magnetic field through the interpolation method, we follow Lehe et al. (2009) in replacing the interpolated electric field with the quantity

$$\tilde{\mathbf{E}} = \overline{\mathbf{E}} + \frac{(\overline{\mathbf{E}} \cdot \overline{\mathbf{B}} - \overline{\mathbf{E}} \cdot \overline{\mathbf{B}})}{\|\overline{\mathbf{B}}\|^2} \overline{\mathbf{B}}, \quad (21)$$

so that  $\tilde{\mathbf{E}} \cdot \overline{\mathbf{B}} = \overline{\mathbf{E}} \cdot \overline{\mathbf{B}}$ , where the overlines stand for the TSC interpolation. Since  $\mathbf{E}$  is perpendicular to  $\mathbf{B}$  on the gridpoints of the RMHD simulation, the electric field seen by the particle is perpendicular to the interpolated magnetic field.

We initialize the particles with random velocities drawn from a Maxwellian distribution and with positions uniformly distributed throughout the numerical domain. Before we introduce the test particles into a simulation, we calculate the velocity power spectrum  $E_u(k_\perp)$  and the rms amplitude of the fluctuating velocity  $u_{\text{rms}}$  using a time average of the simulation data over the time interval  $(t_1, t_2)$ , where  $t_1$  is some time after the turbulence has reached an approximate statistical steady state, and  $t_2$  is the time at which the particles are

introduced, which satisfies  $t_2 > t_1$ . For example, in Simulations D1 through D5 of Table 1,  $t_1 = t_{\text{RMHD}} + 14L_{\perp}/u_{\text{rms}}$  and  $t_2 = t_{\text{RMHD}} + 25L_{\perp}/u_{\text{rms}}$ , where  $t_{\text{RMHD}}$  is the beginning of the RMHD simulation. To determine  $v_{\perp i}$  and  $\Omega_i$ , we then proceed through the following steps. First, we pick a value for  $\rho_i/L_{\perp}$ , which fixes the value of  $\delta u/u_{\text{rms}}$  through Equations (6) and (13). Second, we choose the value of  $\varepsilon$  that we wish to simulate. The values of  $\varepsilon = \delta u/v_{\perp i}$  and  $\delta u/u_{\text{rms}}$  fix the value of  $v_{\perp i}/u_{\text{rms}}$ , while the values of  $v_{\perp i}/u_{\text{rms}}$  and  $\rho_i/L_{\perp}$  determine the gyrofrequency  $\Omega_i = v_{\perp i}/\rho_i$  in units of  $u_{\text{rms}}/L_{\perp}$ . Third, we choose the value of  $\beta_i$ , which is defined in Equation (8), for the initial particle distribution. Because  $v_{\perp i}/u_{\text{rms}}$  is already fixed from the first two steps above, we need to vary  $u_{\text{rms}}/v_A$  in order to vary  $\beta_i$ . Here, we make use of the fact that the RMHD equations are invariant when we multiply both  $v_A$  and  $L_{\parallel}$  by the same scaling factor. For an RMHD simulation with some given value of  $v_A/u_{\text{rms}}$  and  $L_{\parallel}/L_{\perp}$ , we re-scale both  $v_A$  and  $L_{\parallel}$  before passing the field variables to the particle integrator in order to achieve the desired value of  $\beta_i$ .

Because we need high accuracy to ensure that the changes of the particles' magnetic moments are not the result of numerical errors, the time steps of the test-particle integration are smaller than the time steps of the RMHD code (by a factor that is typically  $\simeq 4$ ). We run the test-particle code and RMHD code at the same time so that we can update the field information for the particles as often as needed without saving the full time history of the RMHD fields to memory. To save computational resources, we use a single RMHD simulation to simulate, simultaneously, several different cohorts of particles, where each cohort corresponds to a different choice of the parameters  $\rho_i/L_{\perp}$ ,  $\varepsilon$ , and  $\beta_i$ . In particular, each simulation designation in Table 1 (e.g., D1, D2, etc.) corresponds to several different test-particle cohorts (each with a different value of  $\varepsilon$ ) within the same RMHD simulation.

We define  $N$  to be the number of particles in each cohort of particles. We estimate the numerical error associated with finite particle number  $N$  by measuring the difference between the heating rate determined using  $N$  particles and the heating rate determined using  $N/2$  particles. We find that this error is  $\simeq 5\%$  for  $N = 5.12 \times 10^4$ . We use  $N \simeq 10^5$  in the simulation results reported in Section 5.

#### 4.3. Charge-to-Mass Ratios, Physical Lengthscales, and the RMHD Assumptions

The test particles in our simulations can represent any ion species. Fundamentally, this is because physical lengthscales such as the proton gyroradius and proton inertial length do not enter into the RMHD equations. There are thus several “hidden” parameters whose values we are free to adjust in order to make the test particles correspond to protons, alpha particles, or a minor-ion species. For example, after fixing the values of the dimensionless quantities  $\rho_i/L_{\perp}$ ,  $\varepsilon$ , and  $\beta_i$  as described at the end of Section 4.2, we can assign an arbitrary physical value to  $\delta u$ , which translates into physical values for  $v_{\perp i}$  and  $v_A$  through our choices of  $\varepsilon$  and  $\beta_i$ . We are free to assign any physical value to the proton mass density  $n_p m_p$ ; the values of  $n_p m_p$  and  $v_A$  then yield the value of  $B_0$  through Equation (1). We can then assign any physical value to  $L_{\perp}$ . Since the values of  $v_{\perp i}$  and  $\rho_i/L_{\perp}$  have already been specified, the value of  $L_{\perp}$  determines the physical value of  $\Omega_i$ . Combining  $\Omega_i$  and  $B_0$  yields the charge-to-mass ratio  $q/m$ , which can take on any value that we choose. In addition, because we can separately assign arbitrary physical values to

both  $\delta u$  and  $L_{\perp}$ , we can choose the the test-particle ions to be any species we like and simultaneously take the inverse proton gyroradius to correspond to any desired multiple of the dissipation wavenumber  $k_d$  of the turbulence power spectrum, which is defined in Equation (27) below.

If we take  $k_d$  to correspond to the spectral break at wavenumbers  $\sim \rho_p^{-1}$  in the magnetic power spectrum in the solar wind, then the perpendicular box size in the largest of our simulations (Simulations D1 through D5 of Table 1) is 150 times larger than the wavelength  $2\pi/k_d$  corresponding to  $k_d$ . Because the inertial range spans more than three orders of magnitude in wavenumber in the solar wind at  $r \lesssim 1$  AU, our RMHD simulations approximate just a portion of the inertial range — the largest  $\sim 2$  orders of magnitude of wavenumbers just below  $k_d$ .

As mentioned at the beginning of Section 3, one of the assumptions of RMHD is that the rms amplitude of the magnetic-field fluctuations  $\delta B_{\text{rms}}$  satisfies

$$\delta B_{\text{rms}} \ll B_0. \quad (22)$$

We can write the ratio  $\delta B_{\text{rms}}/B_0$  in the form

$$\frac{\delta B_{\text{rms}}}{B_0} = \left( \frac{\delta B_{\text{rms}} v_A}{B_0 u_{\text{rms}}} \right) \left( \frac{u_{\text{rms}}}{\delta u} \right) \varepsilon \beta_i^{1/2}. \quad (23)$$

The quantities  $\delta B_{\text{rms}}$  and  $u_{\text{rms}}$  are the total rms values of the fluctuating magnetic field and velocity, respectively, including contributions from all values of  $k_{\perp}$ . The first term on the right-hand side of Equation (23),  $\delta B_{\text{rms}} v_A / (B_0 u_{\text{rms}})$ , is  $\simeq 1.4$  in our simulations. The second term on the right-hand side of Equation (23),  $u_{\text{rms}}/\delta u$ , is  $\simeq 2.2$ . In our simulations with  $\beta_i < 0.2$ , we restrict  $\varepsilon$  to values  $\lesssim 0.25$ . This restriction leads to small values of  $\delta B_{\text{rms}}/B_0$  in our simulations with  $\beta_i = 0.006$ , specifically,

$$\frac{\delta B_{\text{rms}}}{B_0} < 0.07 \quad (\text{at } \beta_i = 0.006). \quad (24)$$

In our larger- $\beta_i$  simulations, on the other hand, Equation (22) is less well satisfied. The most problematic case is our  $\beta_i = 1$  simulations, in which we restrict  $\varepsilon$  to values smaller than 0.157, leading to a maximum value of  $\delta B_{\text{rms}}/B_0$  of 0.47, so that

$$\frac{\delta B_{\text{rms}}}{B_0} \leq 0.47 \quad (\text{at } \beta_i = 1). \quad (25)$$

We return to this issue when we discuss Figures 7 and 8 below.

Another assumption in RMHD that was mentioned at the beginning of Section 3 is that the lengthscales are much larger than  $\rho_p$ . The application of our simulations to the stochastic heating of thermal protons is thus approximate at best, and some caution must be exercised when making inferences about stochastic proton heating based on this work. The use of RMHD simulations is more justified for heavy ions whose gyroradii exceed  $\rho_p$ . To treat the stochastic heating of thermal protons more rigorously, a numerical approach that accounts for kinetic processes at lengthscales  $\sim \rho_p$  is needed — e.g., gyrokinetic simulations, hybrid simulations, or particle-in-cell simulations. An advantage of RMHD, and one of the reasons we use it here, is that it is possible to simulate a large dynamic range in three dimensions in RMHD while simultaneously focusing computational resources on highly anisotropic fluctuations with  $k_{\perp} \gg k_{\parallel}$ . This large dynamic range makes it possible to explore phenomena such as coherent structures in 3D turbulence, which become increasingly

prominent as the inertial range broadens (Wan et al. 2012a). We return to this point in Section 5.

## 5. RESULTS

We have carried out RMHD simulations for four different grid sizes:  $128^3$ ,  $256^3$ ,  $512^2 \times 256$ , and  $1024^2 \times 256$ . These grid sizes are listed in the format  $N_\perp^2 \times N_\parallel$ , where  $N_\parallel$  is the number of grid points along the direction of the background magnetic field (the  $z$  direction), and  $N_\perp$  is the number of grid points in each of the  $x$  and  $y$  directions. As  $N_\perp$  increases, we decrease the viscosity  $\nu$  so that the Reynolds number  $Re$  increases, where

$$Re = \frac{u_{rms} L_\perp}{\nu}. \quad (26)$$

We inject equal amounts of energy into  $z^+$  and  $z^-$  so that the turbulence is “balanced.” For reference, we define a dissipation wavenumber

$$k_d = \left[ \frac{\int k_\perp^4 E_u(k_\perp) dk_\perp}{\int k_\perp^2 E_u(k_\perp) dk_\perp} \right]^{1/2}. \quad (27)$$

The values of  $k_d$  and  $Re$  in our different RMHD simulations are listed in Table 1. As mentioned in Section 4.2, we track several different cohorts of particles within each RMHD simulation, where each cohort has a different value of  $\varepsilon$  but the same value of  $\beta_i$ .

At  $k_\perp \gtrsim k_d$ , the fluctuations are strongly influenced by dissipation. At much smaller wavenumbers  $\sim 2\pi/L_\perp$ , the fluctuations are strongly influenced by the details of the numerical forcing term  $f^\pm$  in Equation (10). However, in the “inertial range” of wavenumbers satisfying  $(2\pi/L_\perp) \ll k_\perp \ll k_d$ , forcing and dissipation have only a small effect, and the power spectra attain approximately power-law forms. The velocity power spectrum  $E_u$ , magnetic power spectrum  $E_b$ , and total power spectrum  $E_{tot} = (E_u + E_b)/2$ , averaged over two of our  $1024^2 \times 256$  simulations (D1 and D2), are shown in Figure 1. As this figure shows, in the inertial range  $E_{tot} \propto k^{-3/2}$ ,  $E_u$  is somewhat flatter than  $k^{-3/2}$  and  $E_b$  is somewhat steeper than  $k^{-3/2}$ , as in previously published RMHD simulations (Boldyrev et al. 2011).

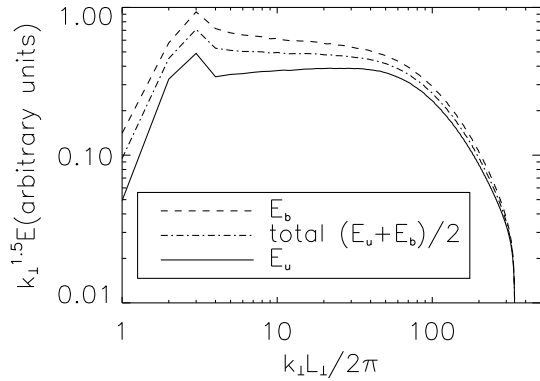


FIG. 1.— The velocity power spectrum  $E_u$ , magnetic power spectrum  $E_b$ , and total-energy spectrum  $(E_u + E_b)/2$  averaged over two of our  $1024^2 \times 256$  simulations (D1 and D2).

To calculate  $Q_\perp$  in our simulations, we measure the mean square values of the particles’ velocity components perpendicular and parallel to the local magnetic field,  $v_\perp$  and  $v_\parallel$ . In Figure 2, we plot  $\langle v_\perp^2 \rangle$  and  $\langle v_\parallel^2 \rangle$  versus time in a  $1024^2 \times 256$  simulation with  $\rho_i = L_\perp/(20\pi)$ ,  $\varepsilon = 0.15$ , and  $\beta_i = 0.006$ . (This figure describes one of the particle cohorts in Simulation D1 of Table 1.) This value of  $\beta_i$  (and all values of  $\beta_i$  listed in Table 1) describe the initial particle distribution. During the first few gyroperiods after the particles are introduced into the simulation,  $\langle v_\perp^2 \rangle$  increases rapidly as the particles “pick up” the  $\mathbf{E} \times \mathbf{B}$  velocity of the turbulence.<sup>4</sup> We neglect this brief period of transient heating when calculating the heating rates. More specifically, we set

$$Q_\perp = \frac{1}{2} \left( \frac{\langle v_{\perp f}^2 \rangle - \langle v_{\perp 0}^2 \rangle}{t_f - t_0} \right), \quad (28)$$

and

$$Q_\parallel = \frac{1}{2} \left( \frac{\langle v_{\parallel f}^2 \rangle - \langle v_{\parallel 0}^2 \rangle}{t_f - t_0} \right), \quad (29)$$

where  $\langle \dots \rangle$  indicates an average over all simulated particles,  $v_{\perp 0}$  ( $v_{\parallel 0}$ ) is a particle’s perpendicular velocity at  $t = t_0$  ( $t = t_\parallel$ ),  $t_0 = 10/\Omega_i$ , and  $t_f$  is either the end of the simulation or the time at which  $\langle v_{\perp f}^2 \rangle = 1.2 \langle v_{\perp 0}^2 \rangle$ . The reason we do not use values of  $t_f$  that are so large that  $\langle v_{\perp f}^2 \rangle > 1.2 \langle v_{\perp 0}^2 \rangle$  is that the heating rate decreases as  $\langle v_{\perp f}^2 \rangle$  increases (Chandran et al. 2010).

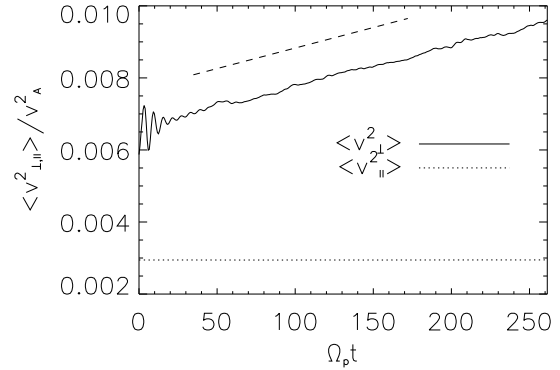


FIG. 2.—  $v_\perp^2$  and  $v_\parallel^2$  vs time for a particle cohort with  $\varepsilon = 0.15$  in Simulation D1. The dashed line indicates the fitting range we use for finding  $Q_\perp$ .

For each value of  $\rho_i/L_\perp$ ,  $\beta_i$ , and  $N_\perp^2 \times N_\parallel$  that we investigate, we simulate  $N_c$  cohorts of particles with different initial values of  $\varepsilon$ . When  $\beta_i < 0.2$ , we use  $N_c = 6$ . When  $\beta_i > 0.2$ , we use  $N_c = 4$  (because we restrict ourselves to a smaller maximum value of  $\varepsilon$  in order to reduce the maximum value of  $\delta B_{rms}/B_0$ , as discussed in Section 4.3). For each cohort, we calculate  $Q_\perp$  using Equation (28). We then fit these values of  $Q_\perp$  to Equation (4), varying  $c_1$  and  $c_2$  to optimize the fit. (Figure 7 illustrates two such fits.) We thus obtain a value of

<sup>4</sup> In the limit of small  $\rho_i$ , the particles would pick up the full  $\mathbf{E} \times \mathbf{B}$  velocity. However, some of the turbulent fluctuations are on scales  $\lesssim \rho_i$ , and the interaction between the particles and these small-scale fluctuations is more complicated than a simple  $\mathbf{E} \times \mathbf{B}$  drift.

$c_1$  and  $c_2$  for each choice of  $\rho_i/L_\perp$ ,  $\beta_i$  and  $N_\perp^2 \times N_\parallel$ . We list the results of our simulations in Table 1, along with several important parameters, including

$$k_p = \frac{1}{\rho_i}. \quad (30)$$

It is fluctuations with  $e^{-0.5}k_p < k_\perp < e^{0.5}k_p$  that determine the value of  $\delta u$  in Equation (6) and hence the value of  $\varepsilon$  in Equations (4) and (5). Because  $\langle v_\perp^2 \rangle$  and  $\delta u$  vary during a simulation, the value of  $\varepsilon$  also varies. When we use our numerical simulations to determine  $Q_\perp$  and  $Q_\parallel$  as functions of  $\varepsilon$ , we calculate  $\varepsilon$  in Equation (5) using the value of  $v_{\perp i}$  at the instant the particles are introduced and the value of  $\delta u$  that is obtained by averaging the velocity power spectrum over the time interval  $(t_0, t_f)$  during which the heating rates are calculated. Thus, the final values of  $\varepsilon$  that are used in, e.g., Figure 7 below, differ slightly from the values of  $\varepsilon$  at the beginning of the test-particle integration.

TABLE 1  
SIMULATION PARAMETERS

Run	Grid Size	Re	$\frac{k_d L_\perp}{2\pi}$	$\frac{k_p L_\perp}{2\pi}$	$\beta_i$	$c_2$	$c_1$
A	$128^3$	2400	29	10	0.006	0.44	0.83
B1	$256^3$	6000	42	10	0.006	0.41	1.0
B2	$256^3$	6000	42	10	0.033	0.41	1.5
B3	$256^3$	6000	42	10	0.18	0.42	1.6
B4	$256^3$	6000	42	10	1.0	0.41	3.6
C1	$512^2 \times 256$	15000	77	10	0.006	0.29	0.80
C2	$512^2 \times 256$	15000	77	20	0.006	0.40	1.1
C3	$512^2 \times 256$	15000	77	20	0.1	0.37	0.86
C4	$512^2 \times 256$	15000	77	20	1.0	0.38	3.7
D1	$1024^2 \times 256$	38000	150	10	0.006	0.20	0.71
D2	$1024^2 \times 256$	38000	150	20	0.006	0.22	0.67
D3	$1024^2 \times 256$	38000	150	40	0.006	0.25	0.62
D4	$1024^2 \times 256$	38000	150	80	0.006	0.21	0.74
D5	$1024^2 \times 256$	38000	150	160	0.006	0.15	0.94

As Table 1 shows, both  $c_1$  and  $c_2$  vary from simulation to simulation. However, because  $c_2$  appears in the argument of the exponential function in Equation (4), the variations in the values of  $c_2$  are particularly important for modeling stochastic heating in the solar corona and solar wind. Much of our focus is thus on how  $c_2$  depends upon simulation size,  $k_p$ , and  $\beta_i$ .

In Figure 3 we plot the values of  $c_2$  in simulations A, B1, C1, and D1 of Table 1. These simulations have the same values of  $k_p L_\perp / (2\pi)$  and  $\beta_i$  (10 and 0.006, respectively), but different values of  $N_\perp$  and Re. This figure shows that  $c_2$  decreases (i.e., stochastic heating becomes stronger) at fixed  $k_p L_\perp$  as  $N_\perp$  and Re increase. As  $N_\perp$  and Re increase at fixed  $k_p L_\perp$ , the inertial range extends to larger wavenumbers relative to  $k_p$  (i.e.,  $k_d/k_p$  increases), and there is more wave power at  $k_\perp \gtrsim k_p$  for any fixed value of  $\varepsilon$ . This additional small-scale power enhances the stochastic heating rate, providing an explanation for the trend in Figure 3.

In Figure 4, we plot the values of  $c_2$  in Simulations B1, C2, and D3. The value of  $N_\perp$  doubles going from Simulation B1 to Simulation C2, and doubles again going from Simulation C2 to Simulation D3. As  $N_\perp$  doubles, the Reynolds

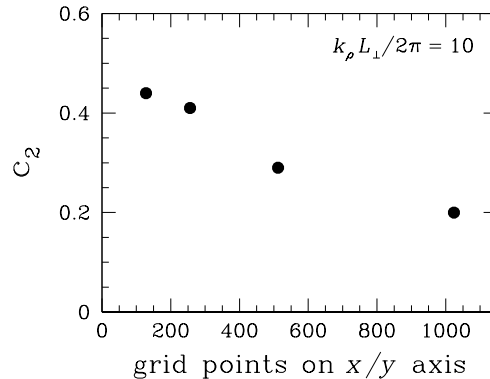


FIG. 3.— The dependence of  $c_2$  on grid resolution (and Re — see Table 1) at fixed  $k_p = 10$ . The data points are from Simulations A, B1, C1, and D1 in Table 1. In these simulations,  $\beta_i = 0.006$ .

number is increased in such a way that the value of  $k_d L_\perp$  also approximately doubles in these simulations. For the simulations shown in Figure 4, we double  $k_p L_\perp$  each time  $N_\perp$  doubles, so that  $k_p/k_d$  remains approximately constant. As this figure shows, doubling  $k_p L_\perp$  while keeping  $k_p/k_d$  constant causes  $c_2$  to decrease, so that stochastic heating becomes more effective. There are likely two reasons for this. First, as  $k_p L_\perp$  increases at fixed  $k_p/k_d$ , there is extra fluctuation energy at  $k_\perp < k_p$  in the RMHD simulation, and this additional fluctuation energy contributes to some extent to particle heating. Second, as  $k_p L_\perp$  increases, coherent structures become more prevalent at the ion-gyroradius scale. Coherent structures, such as current sheets, become increasingly prevalent at smaller scales within the inertial range (Wan et al. 2012a). This phenomenon can be seen in Figure 5, where we plot the kurtosis  $K$  as a function of  $k_\perp$  in Simulations B1-B4, C1-C4, and D1-D5. The kurtosis is a measure of coherent structures or non-Gaussianity. For a distribution of  $n$  vectors  $\mathbf{x}_j$  with  $j = 0, 1, 2, \dots, n-1$ , the kurtosis is given by

$$K = \frac{1}{n} \sum_{j=0}^{n-1} \left| \frac{\mathbf{x}_j - \bar{\mathbf{x}}}{\sigma} \right|^4 - 3, \quad (31)$$

where  $\bar{\mathbf{x}} = n^{-1} \sum_{j=0}^{n-1} \mathbf{x}_j$  and  $\sigma = [(n-1)^{-1} \sum_{i=0}^{n-1} |\mathbf{x}_i - \bar{\mathbf{x}}|^2]^{1/2}$ . In this problem, the individual vectors  $\mathbf{x}_j$  are of the form  $\mathbf{x}_j = \mathbf{z}^\pm(\mathbf{r} + \mathbf{l}) - \mathbf{z}^\pm(\mathbf{r})$ , where the  $\mathbf{r}$  vectors locate a set of evenly spaced grid points (separated by eight grid points in each Cartesian direction), the separation vector  $\mathbf{l}$  is given by either  $\mathbf{l} = \hat{\mathbf{x}}\pi/k_\perp$  or  $\mathbf{l} = \hat{\mathbf{y}}\pi/k_\perp$ , and  $k_\perp$  is varied. In our strong RMHD turbulence simulations,  $K$  increases steadily with increasing  $k_\perp$ , reaching values  $\simeq 5$  at  $k_\perp L_\perp / 2\pi \simeq 70$ . The importance of coherent structures in turbulent heating has been discussed by a number of authors (e.g., Dmitruk et al. 2004; Wan et al. 2010; Parashar et al. 2011; Markovskii & Vasquez 2011; Servidio et al. 2011b, 2012; Greco et al. 2012; TenBarge & Howes 2013; Haynes et al. 2013; Karimabadi et al. 2013; Wu et al. 2013). The reason that coherent structures enhance stochastic heating was described by Chandran et al. (2010). As the turbulent heating is concentrated into a smaller volume in which the fluctuation amplitudes are larger, the particle orbits become more stochastic at the locations where the heating occurs.

In Figure 6, we show how  $c_2$  depends upon the value

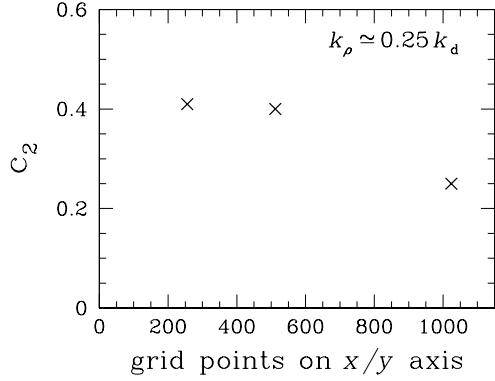


FIG. 4.— The dependence of  $c_2$  on grid resolution (and  $\text{Re}$  — see Table 1) at fixed  $k_p/k_d \simeq 0.25$ . The data points are from Simulations B1, C2, and D3 in Table 1. In these simulations,  $\beta_i = 0.006$ .

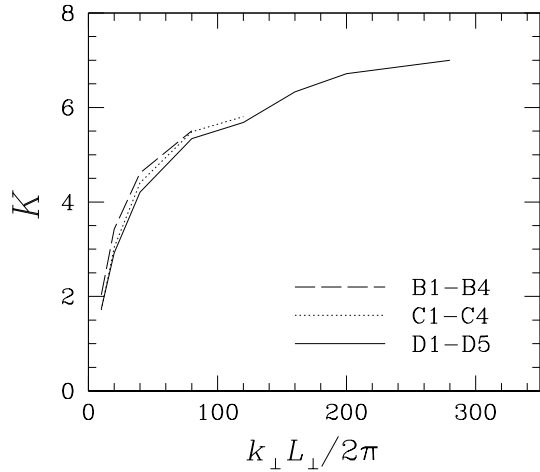


FIG. 5.— Kurtosis  $K$  as a function of  $k_\perp$  in Simulations B1-B4, C1-C4, and D1-D5.

of  $k_p$  in our  $1024^2 \times 256$  simulations. The data points in this figure correspond to Simulations D1 through D5 in Table 1. This figure appears to show a competition between the effects described above. As  $k_p L_\perp / (2\pi)$  increases from 10 to 40, there are fewer modes with  $k_\perp$  exceeding  $k_p$  within the RMHD simulations, and thus fewer sub-gyroradius-scale fluctuations contribute to the stochastic heating of the test particles. We conjecture that this is why  $c_2$  increases in Figure 6 as  $k_p L_\perp / (2\pi)$  increases from 10 to 40. On the other hand, as  $k_p L_\perp / (2\pi)$  increases above 40, the trend reverses and  $c_2$  decreases. We conjecture that this decrease occurs because two other effects discussed above become dominant: the increasing prevalence of coherent structures at  $k_\perp = k_p$  and the increasing contribution to  $Q_\perp$  from fluctuations with  $k_\perp \ll k_p$ . This latter effect becomes increasingly important as  $k_p$  increases to values  $\gtrsim k_d$ . In this case,  $\delta u$  becomes so small that even a modest contribution to  $Q_\perp$  from fluctuations with  $k_\perp \ll k_p$  leads to a significant decrease in  $c_2$  and/or increase in  $c_1$ .

Figure 6 implies that there is some variation in the value of  $c_2$  for different ion species. For example, if ion temperatures are mass proportional, then  $k_p \propto q/m$ . In this case, if the

point with  $k_p L_\perp / 2\pi = 80$  in Figure 6 represents protons, then the point with  $k_p L_\perp / 2\pi = 40$  corresponds to alpha particles. However, some caution is warranted when attempting to infer the species dependence of  $c_2$  from Figure 6. As discussed in Sections 4.3 and 6, our RMHD simulations neglect kinetic effects that arise at scales  $\lesssim \rho_p$ , which presumably have a larger effect on the value of  $c_2$  for protons than on the value of  $c_2$  for heavy ions with gyroradii exceeding  $\rho_p$ .

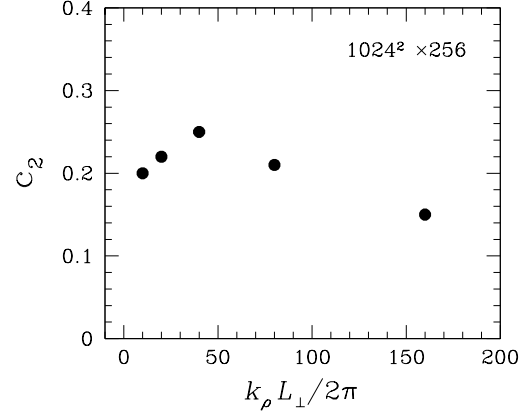


FIG. 6.— The value of  $c_2$  in Simulations D1 through D5, in which  $\beta_i = 0.006$ . The gyroradius  $\rho_i = k_p^{-1}$  takes on a different value in each simulation.

Figure 7 shows the relative strength of parallel heating and perpendicular heating as a function of  $\epsilon$  for two different values of  $\beta_i$ . Because ideal RMHD fluctuations possess a magnetic-field-strength fluctuation that is second order in the fluctuation amplitude ( $\delta|B|/B_0 \sim (|\delta\mathbf{B}|/B_0)^2$ ) and have no parallel electric field, Landau/transit-time damping (LD/TTD) is weaker than it would be in, e.g., fast magnetosonic turbulence with the same rms value of  $|\delta\mathbf{B}|/B_0$ . Nevertheless, as these figures show, some parallel heating does occur. Figure 7 shows that  $Q_\parallel/Q_\perp$  is larger when  $\beta_i \sim 1$  than when  $\beta_i \sim 0.006$ . This is in part because when  $\beta_i \ll 1$ , the ions are too slow to “surf” effectively on the RMHD fluctuations, even accounting for the resonance broadening that arises from the nonlinear decorrelation of the fluctuations (Lehe et al. 2009; Lynn et al. 2012). We note that our simulation method does not provide a realistic assessment of parallel heating by low-frequency Alfvén-wave turbulence in the solar wind, because such turbulence likely becomes KAW turbulence at perpendicular scales  $\lesssim \rho_p$ . KAW fluctuations involve magnetic-field-strength fluctuations that are first order in the fluctuation amplitude ( $\delta|B|/B_0 \sim |\delta\mathbf{B}|/B_0$ ). Parallel heating from LD/TTD is thus much stronger for KAW turbulence than it is for RMHD turbulence.

As mentioned in Section 4.3, when  $\beta_i = 1$ , we restrict our simulations to  $\epsilon \lesssim 0.15$  in order to reduce the maximum value of  $\delta B_{\text{rms}}/B_0$ . This is why the results from Simulation C4 in Figure 7 are limited to smaller  $\epsilon$  values than the results from Simulation C2. Despite this restriction, the value of  $\delta B_{\text{rms}}/B_0$  reaches a maximum value of 0.47 in the  $\beta_i = 1$  simulation with  $\epsilon \simeq 0.15$ . This value of  $\delta B_{\text{rms}}/B_0$  is not  $\ll 1$ , as required in RMHD, and thus our  $\beta_i = 1$  results must be viewed with some caution. For example, because  $\delta B_{\text{rms}}/B_0 \simeq 1/2$  in our simulation with  $\beta_i = 1$  and  $\epsilon_i \simeq 0.15$ , the magnetic field lines in this simulation are tilted by  $\simeq 30^\circ$  with respect to



the  $z$  direction. The small-scale structure in the  $xy$ -plane in this simulation may thus lead to small-scale structure parallel to the local magnetic field lines (but see Cho & Vishniac 2000). As a consequence, some of the perpendicular heating in this simulation may result from a Doppler-shifted cyclotron resonance. Alternative simulation techniques, including test-particle simulations based on incompressible MHD rather than RMHD, would be useful for further investigations into stochastic-heating at  $\beta_i = 1$ .

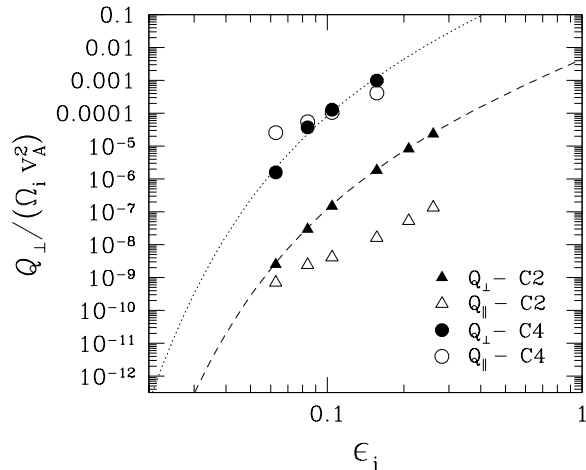


FIG. 7.—  $Q_{\perp}$  and  $Q_{\parallel}$  as functions of  $\epsilon_i$  in Simulation C2 (in which  $\beta_i = 0.006$ ) and Simulation C4 (in which  $\beta_i = 1$ ). The dashed line is a plot of Equation (4) with  $c_1 = 1.1$  and  $c_2 = 0.4$ , and the dotted line is a plot of Equation (4) with  $c_1 = 3.7$  and  $c_2 = 0.38$ . This plot shows that  $Q_{\parallel}/Q_{\perp}$  increases as  $\beta_i$  increases.

In Figure 8 we plot the values of  $c_1$  and  $c_2$  in several simulations with different values of  $\beta_i$ . As  $\beta_i$  increases from 0.006 to 1,  $c_2$  undergoes only small variations, but  $c_1$  increases by a factor of  $\sim 3$ . These trends indicate that stochastic heating becomes more effective at fixed  $\delta u$ ,  $\rho_i$ , and  $\epsilon_i$  as  $\beta_i$  is increased from 0.006 to 1. However, as discussed above, our results on the  $\beta_i = 1$  case must be viewed with caution, since  $\delta B_{\text{rms}}/B_0$  reaches values as large as 0.47.

## 6. DISCUSSION AND CONCLUSION

In this paper, we describe numerical simulations of test-particles interacting with strong RMHD turbulence. By tracking the change in particle energy with time, we evaluate the stochastic heating rate  $Q_{\perp}$  as a function of the amplitude of the turbulent fluctuations at the gyroradius scale. Our results for  $Q_{\perp}$  are well described by the functional form in Equation (4), which was derived by Chandran et al. (2010) using phenomenological arguments. Our simulations enable us to evaluate the constants  $c_1$  and  $c_2$  in this equation for strong RMHD turbulence, and to determine how these constants depend upon various properties of the turbulence and particle distributions.

We find that strong RMHD turbulence is much more effective than randomly phased waves at stochastically heating ions, in the sense that the constant  $c_2$  in Equation (4) is significantly smaller for ions interacting with strong RMHD turbulence than for ions interacting with randomly phased waves. This difference likely arises because of the coherent structures

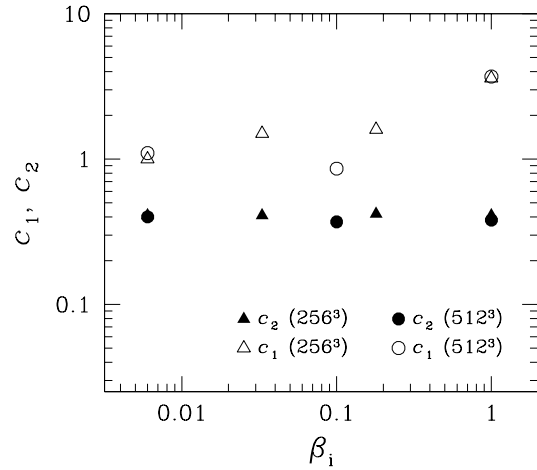


FIG. 8.—  $c_1$  and  $c_2$  vs  $\beta_i$  in Simulations B1 to B4 (triangles) and Simulations C2 to C4 (circles).

that develop in strong RMHD turbulence, whose prevalence is measured by the kurtosis  $K$  in Equation (31). The fluctuation amplitudes are larger in the vicinity of coherent structures, which increases orbit stochasticity. This enables particles to absorb more energy from the time-varying electrostatic potential in the regions where most of the particle heating occurs. We also find that the constants  $c_1$  and  $c_2$  undergo small variations as  $\beta_i$  increases from 0.006 to 1, in the sense that stochastic heating becomes moderately more effective for fixed values of  $\delta u$ ,  $\rho_i$ , and  $\epsilon_i$ . This implies that stochastic heating can occur not only in the low- $\beta_i$  conditions of the solar corona but also in the  $\beta_i \sim 1$  conditions found in the solar wind near Earth. Furthermore, we find that the parallel proton heating rate  $Q_{\parallel}$  is much smaller than  $Q_{\perp}$  when  $\beta_i \ll 1$  for the range of  $\epsilon$  values that we have investigated. On the other hand,  $Q_{\parallel}$  can exceed  $Q_{\perp}$  in our simulations for  $\beta \sim 1$  and  $\epsilon \lesssim 0.1$ . As discussed in Section 5, our simulations underestimate the amount of parallel heating in solar-wind turbulence, because we do not take into account the change in the polarization properties of the fluctuations at  $k_{\perp} \rho_p \simeq 1$ , where the AW cascade transitions into a KAW cascade (Bale et al. 2005; Howes et al. 2008b; Sahraoui et al. 2009; Schekochihin et al. 2009).

Our largest runs are Simulations D1 through D5. The values of  $c_2$  in these simulations are  $\sim 0.2$ . On the other hand, the value of  $c_2$  steadily decreases as we increase the number of grid points and Reynolds number, whether we hold constant  $k_p L_{\perp}$  or  $k_p/k_d$ . If we were able to simulate RMHD turbulence with an inertial range as broad as that found in the solar wind, then the resulting values of  $c_2$  would be smaller than the values that we have found in Simulations D1 through D5.

Previous studies have found that  $c_2$  values of order or slightly smaller than 0.2 are required in order for stochastic heating to explain the observed ion temperatures in fast-solar-wind streams and coronal holes. For example, Bourouaine & Chandran (2013) used *Helios* magnetometer data to measure the amplitudes of the gyroscale magnetic-field fluctuations in fast-solar-wind streams at heliocentric distances between 0.29 and 0.64 AU. Given these amplitudes, these authors found that values of  $c_2$  of  $\simeq 0.2$  were sufficient for stochastic heating to explain the non-adiabatic perpendicular proton temperature profile measured by *Helios*. These authors were unable to determine the precise value of  $c_2$  that

is required, however, because of the uncertainty in the assumed relationship between the amplitude of the gyroscale magnetic field fluctuation and the amplitude of the gyroscale  $\mathbf{E} \times \mathbf{B}$  velocity. Chandran (2010) used an approximate model of RMHD-like turbulence in the extended solar atmosphere with  $E_u \propto k_{\perp}^{-3/2}$  and found that stochastic heating could explain observations of  $O^{+5}$  and proton temperatures in coronal holes if  $c_1 \simeq 1$  and  $c_2 = 0.15$ . Chandran et al. (2011) assumed that  $c_1 = 0.75$  and  $c_2 = 0.17$  in a two-fluid (proton/electron) solar-wind model that incorporated Alfvén-wave turbulence, stochastic heating, and proton temperature anisotropy and obtained a reasonable match between the model perpendicular proton temperatures and observations of coronal holes and fast solar-wind streams.

The approximate correspondence between the values of  $c_2$  in our  $1024^2 \times 256$  simulations and the values of  $c_2$  that are needed to explain observed ion temperatures suggests that stochastic heating plays an important role in the solar wind and coronal holes. However, there are several reasons why the rate of stochastic heating in the solar wind might differ from the rate in our numerical simulations. First, we have only considered test particles and have not accounted for the back reaction of the particles upon the turbulence. Second, by considering RMHD turbulence, we neglect the kinetic-Alfvén-wave (KAW) physics that arises at  $k_{\perp} \rho_p \gtrsim 1$ . In KAW turbulence, the electric-field power spectrum flattens as  $k_{\perp}$  increases above  $\rho_p^{-1}$  (Bale et al. 2005), and the additional electric-field power at  $k_{\perp} \rho_p > 1$  presumably enhances

stochastic proton heating in AW/KAW turbulence above the level in RMHD turbulence with the same value of  $\delta u$ . Third, we have neglected the effects of cross helicity or “imbalance” (which arises, e.g., when more Alfvén waves propagate away from the Sun than toward the Sun) and differential flow between ion species (but see Chandran et al. 2013). Future work, including numerical simulations, that accounts for this additional physics will be important for advancing our understanding of stochastic heating further.

Finally, we note that a number of studies find that sheet-like concentrations of current density play an important role in the dissipation of solar-wind turbulence (e.g., Dmitruk et al. 2004; Servidio et al. 2011b; Wan et al. 2012b; Karimabadi et al. 2013). Although these structures are not singular, they are some times referred to as “current sheets.” Our results are consistent with these studies, in the sense that we find that coherent structures enhance the stochastic heating rate.

We thank Peera Pongkitiwanchakul and the anonymous referee for helpful suggestions and comments. This work was supported in part by NSF grant AGS-0851005, NSF/DOE grant AGS-1003451, DOE grant DE-FG02-07-ER46372, and NASA grants NNX07AP65G, NNX08AH52G, NNX11AJ37G and NNX12AB27G. B. Chandran was supported by a Visiting Research Fellowship from Merton College, University of Oxford. E. Quataert was supported by a Simons Investigator award from the Simons Foundation, the David and Lucile Packard Foundation, and the Thomas Alison Schneider Chair in Physics at UC Berkeley.

#### REFERENCES

- Antonucci, E., Dodero, M. A., & Giordano, S. 2000, *Sol. Phys.*, 197, 115
- Bale, S. D., Kellogg, P. J., Mozer, F. S., Horbury, T. S., & Reme, H. 2005, *Physical Review Letters*, 94, 215002
- Boldyrev, S. 2005, *ApJ*, 626, L37
- Boldyrev, S., Perez, J. C., Borovsky, J. E., & Podesta, J. J. 2011, *ApJ*, 741, L19
- Boldyrev, S., Perez, J. C., & Zhdankin, V. 2012, in *American Institute of Physics Conference Series*, Vol. 1436, American Institute of Physics Conference Series, ed. J. Heerikhuisen, G. Li, N. Pogorelov, & G. Zank, 18–23
- Boris, J. 1970, in *Proceedings of the Fourth Conference on Numerical Simulation of Plasmas* (Naval Research Lab), 3–67
- Bourouaine, B., & Chandran, B. 2013, accepted, *Astrophys. J.*
- Chandran, B., Verscharen, D., Quataert, E., Kasper, C., Isenberg, P., & Bourouaine, B. 2013, submitted, *Astrophys. J.*
- Chandran, B. D. G. 2010, *ApJ*, 720, 548
- Chandran, B. D. G., Dennis, T. J., Quataert, E., & Bale, S. D. 2011, *ApJ*, 743, 197
- Chandran, B. D. G., Li, B., Rogers, B. N., Quataert, E., & Germaschewski, K. 2010, *ApJ*, submitted, (arXiv:1001.2069)
- Chaston, C. C., Bonnell, J. W., Carlson, C. W., McFadden, J. P., Ergun, R. E., Strangeway, R. J., & Lund, E. J. 2004, *Journal of Geophysical Research* (Space Physics), 109, 4205
- Chen, L., Lin, Z., & White, R. 2001, *Physics of Plasmas*, 8, 4713
- Cho, J., & Lazarian, A. 2004, *ApJ*, 615, L41
- Cho, J., & Vishniac, E. T. 2000, *ApJ*, 539, 273
- Coleman, P. J. 1968, *ApJ*, 153, 371
- Cranmer, S. R., & van Ballegoijen, A. A. 2003, *ApJ*, 594, 573
- De Pontieu, B., et al. 2007, *Science*, 318, 1574
- Dmitruk, P., Gómez, D. O., & Matthaeus, W. H. 2003, *Physics of Plasmas*, 10, 3584
- Dmitruk, P., Matthaeus, W. H., & Oughton, S. 2005, *Physics of Plasmas*, 12, 112304
- Dmitruk, P., Matthaeus, W. H., & Seenu, N. 2004, *ApJ*, 617, 667
- Durney, B. R. 1972, *J. Geophys. Res.*, 77, 4042
- Esser, R., Fineschi, S., Dobrzycka, D., Habbal, S. R., Edgar, R. J., Raymond, J. C., Kohl, J. L., & Guhathakurta, M. 1999, *ApJ*, 510, L63
- Fiksel, G., Almagri, A. F., Chapman, B. E., Mirnov, V. V., Ren, Y., Sarff, J. S., & Terry, P. W. 2009, *Physical Review Letters*, 103, 145002
- Goldreich, P., & Sridhar, S. 1995, *ApJ*, 438, 763
- Goldstein, M. L., Roberts, D. A., & Matthaeus, W. H. 1995, *ARA&A*, 33, 283
- Greco, A., Valentini, F., Servidio, S., & Matthaeus, W. H. 2012, *Phys. Rev. E*, 86, 066405
- Hartle, R. E., & Sturrock, P. A. 1968, *ApJ*, 151, 1155
- Haynes, C., Burgess, D., & Camporeale, E. 2013, in *EGU General Assembly Conference Abstracts*, Vol. 15, EGU General Assembly Conference Abstracts, 10847
- Hollweg, J. V., & Isenberg, P. A. 2002, *Journal of Geophysical Research* (Space Physics), 107, 1147
- Howes, G. G., Cowley, S. C., Dorland, W., Hammett, G. W., Quataert, E., & Schekochihin, A. A. 2008a, *Journal of Geophysical Research* (Space Physics), 113, 5103
- Howes, G. G., Dorland, W., Cowley, S. C., Hammett, G. W., Quataert, E., Schekochihin, A. A., & Tatsuno, T. 2008b, *Physical Review Letters*, 100, 065004
- Iroshnikov, P. S. 1963, *AZh*, 40, 742
- Isenberg, P. A., & Hollweg, J. V. 1983, *J. Geophys. Res.*, 88, 3923
- Johnson, J. R., & Cheng, C. Z. 2001, *Geophys. Res. Lett.*, 28, 4421
- Kadomtsev, B. B., & Pogutse, O. P. 1974, *Soviet Journal of Experimental and Theoretical Physics*, 38, 283
- Karimabadi, H., et al. 2013, *Physics of Plasmas*, 20, 012303
- Kennel, C. F., & Wong, H. V. 1967, *Journal of Plasma Physics*, 1, 75
- Kohl, J., et al. 1998, *ApJ*, 501, L127
- Kolmogorov, A. N. 1941, *Dokl. Akad. Nauk SSSR*, 30, 299
- Kraichnan, R. H. 1965, *Physics of Fluids*, 8, 1385
- Kruskal, M. 1962, *Journal of Mathematical Physics*, 3, 806
- Lehe, R., Parrish, I. J., & Quataert, E. 2009, *ApJ*, 707, 404
- Lynn, J. W., Parrish, I. J., Quataert, E., & Chandran, B. D. G. 2012, *ApJ*, 758, 78
- Markovskii, S. A., & Vasquez, B. J. 2011, *ApJ*, 739, 22
- Markovskii, S. A., Vasquez, B. J., Smith, C. W., & Hollweg, J. V. 2006, *ApJ*, 639, 1177
- Maron, J., & Goldreich, P. 2001, *ApJ*, 554, 1175

- Marsch, E., Schwenn, R., Rosenbauer, H., Muehlhaeuser, K., Pilipp, W., & Neubauer, F. M. 1982b, *J. Geophys. Res.*, 87, 52
- Mason, J., Perez, J. C., Boldyrev, S., & Cattaneo, F. 2012, *Physics of Plasmas*, 19, 055902
- McChesney, J. M., Stern, R. A., & Bellan, P. M. 1987, *Physical Review Letters*, 59, 1436
- Parashar, T. N., Servidio, S., Shay, M. A., Breech, B., & Matthaeus, W. H. 2011, *Physics of Plasmas*, 18, 092302
- Parashar, T. N., Shay, M. A., Cassak, P. A., & Matthaeus, W. H. 2009, *Physics of Plasmas*, 16, 032310
- Parker, E. N. 1958, *ApJ*, 128, 664
- . 1965, *Space Science Reviews*, 4, 666
- Perez, J. C., & Boldyrev, S. 2008, *ApJ*, 672, L61
- . 2009, *Physical Review Letters*, 102, 025003
- Perez, J. C., Mason, J., Boldyrev, S., & Cattaneo, F. 2012, *Physical Review X*, 2, 041005
- Quataert, E. 1998, *ApJ*, 500, 978
- Roberts, P. H., & Soward, A. M. 1972, *Royal Society of London Proceedings Series A*, 328, 185
- Sahraoui, F., Goldstein, M. L., Robert, P., & Khotyaintsev, Y. V. 2009, *Physical Review Letters*, 102, 231102
- Schekochihin, A. A., Cowley, S. C., Dorland, W., Hammett, G. W., Howes, G. G., Quataert, E., & Tatsuno, T. 2009, *ApJS*, 182, 310
- Servidio, S., Greco, A., Matthaeus, W. H., Osman, K. T., & Dmitruk, P. 2011a, *Journal of Geophysical Research (Space Physics)*, 116, 9102
- Servidio, S., Valentini, F., Califano, F., & Veltri, P. 2012, *Physical Review Letters*, 108, 045001
- Servidio, S., et al. 2011b, *Nonlinear Processes in Geophysics*, 18, 675
- Shebalin, J. V., Matthaeus, W., & Montgomery, D. 1983, *Journal of Plasma Physics*, 29, 525
- Strauss, H. R. 1976, *Physics of Fluids*, 19, 134
- TenBarge, J. M., & Howes, G. G. 2013, *ArXiv e-prints*
- Tomczyk, S., McIntosh, S. W., Keil, S. L., Judge, P. G., Schad, T., Seeley, D. H., & Edmondson, J. 2007, *Science*, 317, 1192
- Tu, C., & Marsch, E. 1995, *Space Science Reviews*, 73, 1
- Voitenko, Y., & Goossens, M. 2004, *ApJ*, 605, L149
- Wan, M., Osman, K. T., Matthaeus, W. H., & Oughton, S. 2012a, *ApJ*, 744, 171
- Wan, M., Oughton, S., Servidio, S., & Matthaeus, W. H. 2010, *Physics of Plasmas*, 17, 082308
- Wan, M., et al. 2012b, *Physical Review Letters*, 109, 195001
- Wu, P., et al. 2013, *ApJ*, 763, L30
- Zank, G. P., & Matthaeus, W. H. 1992, *Journal of Plasma Physics*, 48, 85